# Use of Compressive Sensing Techniques for the Rapid Production Test of Commercial Nose-Mounted Radomes in a Robotic Antenna Measurement System

S.F. Gregson[1, 2] C.G. Parini[2]
[1] Next Phase Measurements LLC, CA, USA, stuart.gregson@qmul.ac.uk
[2] Queen Mary University London, London, UK

***Abstract*—The recent trend towards implementing antenna measurement ranges employing multi-axis industrial robotic positioners that provide a near limitless degree of flexibility in terms of measurement types and scan geometries admits possibilities that go far beyond the requirements of classical antenna measurement systems or perhaps even beyond the expectations of those who originally conceived of the system. One recent example involves the use of a dual robotic antenna measurement system for the near-field test and measurement of commercial nose-mounted radomes. Such measurements typically involve extended measurement times due to the need to acquire two-dimensional near-field data to obtain the asymptotic far-fields. This paper introduces a new approach for the production test and verification of commercial nose-mounted radomes that uses a total difference based, sparse sampling technique that aims to accelerate the measurement process to drastically cut the requisite test time. The new algorithm is introduced, simulated results are presented, where it is demonstrated that far-field results with an equivalent multipath level of better than -60dB can be obtained from as few as 1 to 2% of the points required by a classical Nyquist spherical near-field acquisition scheme.**

***Index Terms*—*Compressive Sensing, Sparse Sampling, Spherical Near-Field,* Nose-Mounted, Commercial Radome, Robotic Test System.**

## I. Introduction

Multi-axis robotic antenna measurement systems are highly capable instruments offering the ability of acquiring classical spherical, cylindrical and planar near-field (NF) data, as well as taking extrapolated gain or direct far-field measurements [1, 2, 3, 4, 5]. Additionally, the flexibility provided by such systems allows other types of measurement to be made, with the test and measurement of commercial nose-mounted radomes being one of the more recent, and novel, innovations [6]. In Figure 1 we show a schematic illustration of a commercial nose-mounted radome enclosing a circular aperture array antenna installed on an industrial 6-axis collaborative robot (CoBot) which we see mounted atop a floor-mounted azimuth stage which is employed as the $\phi$-axis of a spherical near-field (SNF) measurement system. To the right of Figure 1 is a second, larger, 6-axis robot which serves to provide the emulated over-head spherical $\theta$-scanning axis. Together, these axes enable the acquisition of standard SNF data which can be readily processed using standard spherical near-field to far-field transformation algorithms [7]. The third robot shown to the left of Figure 1 is not used in this measurement scenario.

The test and measurement requirements for nose-mounted commercial radomes are specified and controlled by the Radio Technical Commission for Aeronautics (RTCA) and are laid out in their standards documents [8, 9, 10]. Here, DO-213A specifies the minimum operational performance standard for nose-mounted commercial radomes and admits the use of NF measurement techniques within the evaluation process. However, the large number of mechanical pointing angles that the weather radar is required to be positioned in during the radome measurement campaign means that total test times can be somewhat extensive, making techniques for providing faster acquisitions highly desirable.

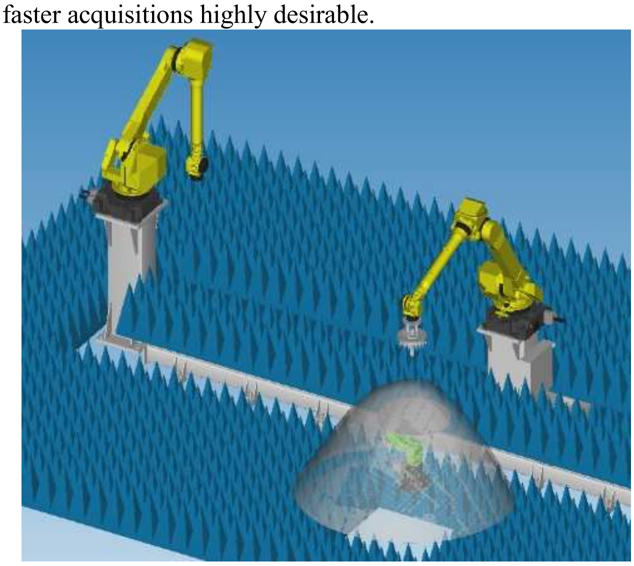

Fig. 1. Illustration of the new dual 6-axis robotic antenna measurement system shown with new nose-radome upgrade.

Compressive Sensing (CS) and Sparse Sampling (SS) based techniques have been deployed in a variety of free-field antenna metrology applications which include radar imaging [11], cylindrical [12] and spherical near-field measurements [13], far-field reflection suppression [14], and for array antenna measurements and diagnostics [15, 16]. Many of these rely upon the inherent sparsity of the associated modal bases [12, 13, 14]. However, that is not necessarily sufficient

978-88-31299-10-7/25/$31.00 ©2025 IEEE

in all cases and thus, a total-difference based approach, analogous to that which is employed by Magnetic Resonance Imaging (MRI) scanners can become an attractive strategy [15, 16]. Recently, this approach has been successfully applied to the SNF case, where it was demonstrated that it could be effectively used to characterize electrically large, electronically scanned, active array antennas using SNF data employing an equivalent current (EC) based algorithm [17].

## II. Overview of CS Based Radome Processing

A detailed treatment of the total-difference, EC based, CS method for the planar and spherical acquisition geometries can be found presented in the open literature, *e.g.* [16, 17], and, because of space restrictions, the derivation is not repeated here. Instead, an overview of the method is provided. To summarise, we first exploit the fact that we are working in a production test and verification environment where we can rely upon the existence of a ‘gold’ reference antenna to undertake a back propagation to the antenna’s aperture from the near-field, or far-field, measurement of the *difference* between the measurement of the, assumed defective, production test antenna, and the assumed ideal ‘gold’ reference. Adhering to the restricted isometry property (RIP) [15], this is accomplished using a small ensemble of, randomly located, measurements. Here, the intention is to minimise the number of measurement points, $M$, required to accurately and reliably measure the test article in the NF, whilst accurately reconstructing the array antenna’s radiating element excitations. However, in this paper, and in contrast to prior works in this area of application, rather than attempting to reconstruct an antenna’s aperture excitations, we are instead attempting to reconstruct a discrete set of magnetic surface currents that are distributed across the non-canonical exterior surface of the radome under test. In principle, it would be possible to examine the excitations of the array antenna, or perhaps the spherical mode coefficients (SMC) of the measurement as a whole. However, as it is the radome that is under investigation, and is that which is assumed to be changing by virtue of being defective, neither of these domains are in fact truly sparse, as a result of spatial diffraction, and therefore greatly limiting the ability of CS and SS based techniques to be successfully deployed using these domains.

By way of an illustration, Figure 2 presents an overview of the data processing and verification chain. Here, we commence by using a model of a slotted waveguide array antenna which is situated behind a perfect radome. We then compute the fields illuminating the radome before propagating those fields to a spherical near-field measurement surface. In this way, it is possible to perturb the fields on the radome surface to emulate a defective example radome, and thus obtain two SNF measurements that can be used to exercise the new EC based CS processing. We compute the difference field from these simulated measurements and then back propagate these to the radome surface using the EC based CS processing. This allows us to determine the true fields for the defective radome whereupon we can first view those defects before computing the complete, *i.e.* non-sparse, spherical near-fields. These spherical near-fields can then be transformed to the far-field using a standard probe corrected spherical near-field to far-field transformation algorithm [7].

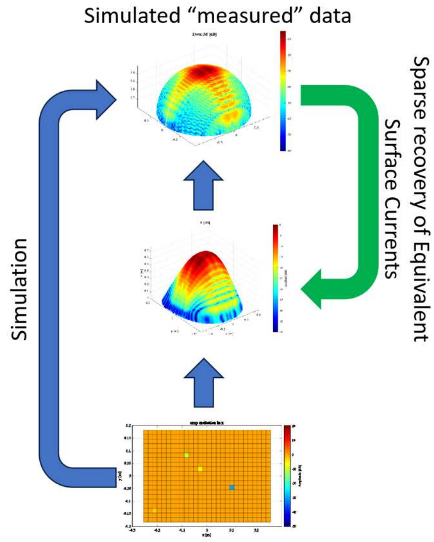


Fig. 2. Schematic representation of the data processing chain utilizing the compressive sensing the recover the equivalent surface currents.

## III. Results

As a starting point Figure 3 shows a modest size radome of 21.9 wavelengths (λ) in diameter and a height of 13.7λ. A SNF surface of radius 24.6λ is also shown. These are fed by a 13×27 element array of λ/2 spaced dipoles. We take 2° spacing in θ and ϕ on the SNF surface and 101×101 grid of points for the back projected radome currents.

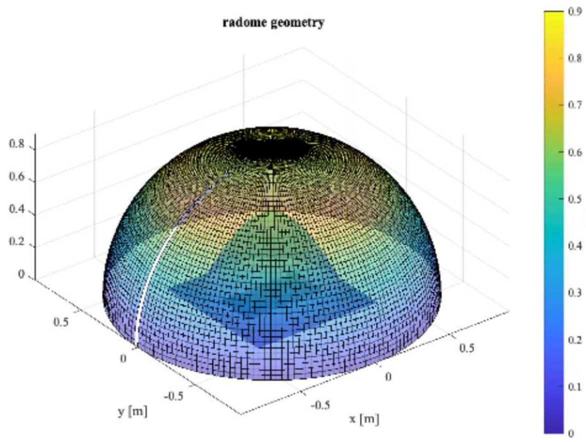


Fig. 3. Array feed, radome and SNF surface geometry for 8.2GHz.

For the case of the ‘gold’ radome if we back project the SNF shown in Figure 2 using the full EC formulation in [17] then solve this system of linear equations using the least squares conjugate gradient LSQR algorithm [7] and compare it to the original radome field of Figure 2, the field is found to be different as shown in Figure 4. However, forward projecting this reconstructed radome field back to the SNF surface accurately reproduces the complete electric spherical near-fields to an RMS accuracy of -64.9 dB. Therefore, the set forms a linear transform pair, but one that does not exactly represent the true radome field.

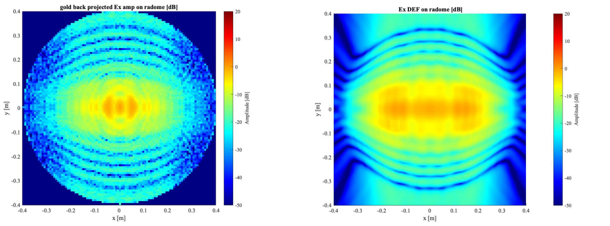

Fig. 4. Comparison of true radome $E_x$ field (right) with that of the back projected field from the SNF surface (left).

However, let us progress with the proposed process of taking the difference between the SNF from the perfect (gold) radome and one that has a defective patch on it over which the field propagated through the radome is changed by a factor of -1 dB and 45° (*i.e.* the defective radome). This difference field is shown in Figure 5, and is sampled with just 100 points (*i.e.* 1.2% of the full classical equiangular SNF requirement) for use with the CS algorithm. These few samples are taken based on a cosine distribution of points in θ from 0° to 90° where, for each θ point, we randomly select a ϕ value between -180° and +180°. This provides weighting with more samples placed in the region with greater field intensities around the SNF pole, and which significantly improves the performance of the CS technique.

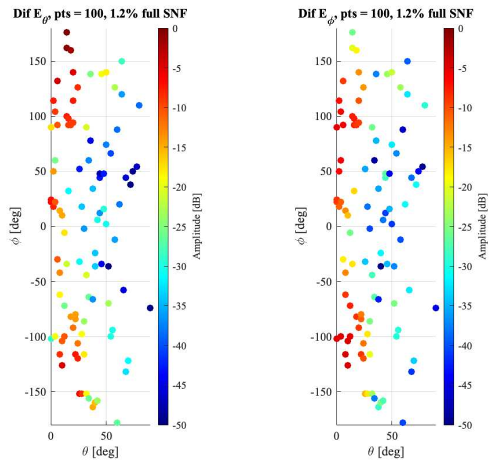


Fig. 5. Difference field between gold and defective radome sparsely sampled across the SNF surface, $E_\theta$ (left), $E_\phi$ (right).

Using the EC based CS processing algorithm of [17] for this SNF case and assuming a simulated measurement noise level of -60 dB, the back projected $x$-polarised difference field on the radome is shown in Figure 6, and which accurately locates the position of the radome defective region. The $E_y$ and $E_z$ fields are also obtained but are not shown here due to space restrictions. It is worth recalling that, in contrast to many prior cases where CS was being employed to determine the complex excitations of an array antenna, for the commercial radome test case under examination here, the exact near amplitude and phase values are of lesser interest than is the *location* of any defect in the radome.

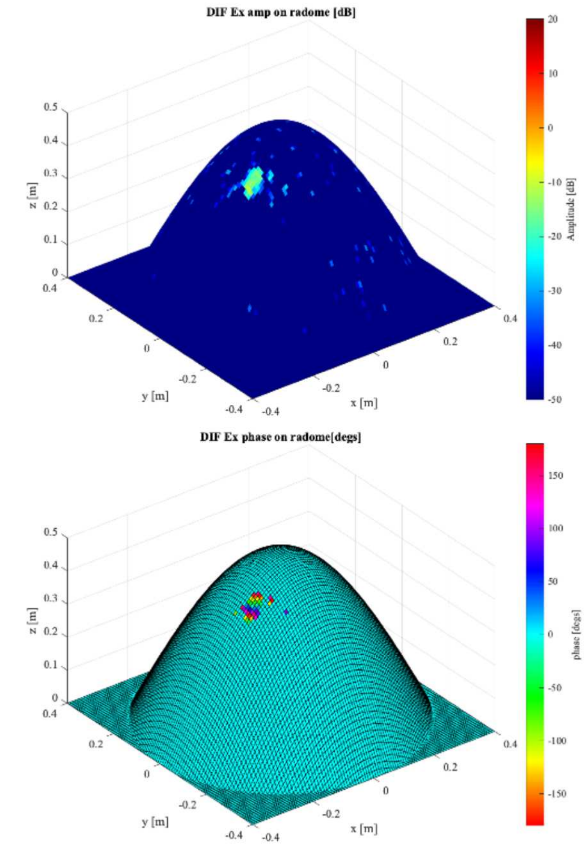


Fig. 6. Difference $E_x$ field between gold and defective radome on the radome surface showing correctly the location of the faulty -1dB and 45° patch. Amplitude (top), Phase (bottom).

Since we know the back projected field of the gold radome from its full SNF measurement (*cf.* Figure 4) we can subtract this from the result of Figure 6 to first reconstruct the defective radome current and then by forward projection we can obtain the complete SNF of the defective radome. The difference between this field and the true defective radome field has an RMS value of -65.1 dB. From this reconstructed defective SNF we can use a conventional SNF to Far-Field (FF) transform to obtain the FF radiation pattern of this reconstructed defective radome and compare it with that which would have been obtained from a conventional, *i.e.* non-sparse, SNF transform of a full measured defective radome, this is shown in Figure 7. The difference between these two FF radiation patterns over the full half sphere (Equivalent Multipath Level – EMPL) is -70.3 dB. Thus, with a known full SNF measurement of the 'gold' radome it is possible to production test the 'faulty' radome with just 99 SNF measurement points and obtain FF radiation patterns with EMPL accuracy of order better than *circa* -60dB as well as being able to locate the position on the radome where the fault (or faults) lay. For this particular radome/antenna combination we found that 100 sample points was the minimum number need to obtain reliable results. The use of a larger number of points gave only marginal improvements in performance and was not used since this would increase the acquisition time which is undesirable.

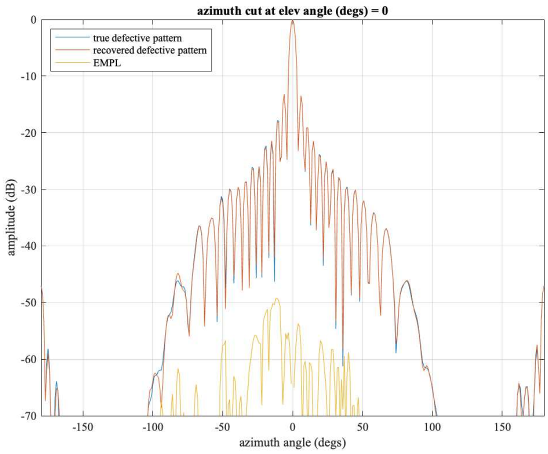


Fig. 7. Comparison of azimuth FF radiation pattern of true defective radome with that of the CS based reconstructed defective radome FF radiation pattern. Also shown is the EMPL which over the full half sphere is -70.3 dB.

## IV. Statistical Assessment of CS Performance

CS is inherently a statistical process and to fully explore the performance of the proposed radome measurement method we need to run the process several times (in this case 50) with a given fault, but with different sets of 100 sample points. For this case, we have chosen to use two faulty patches to illustrate the ability of the process to locate more than a single faulty region. We present the results in Figure 8 using the cumulative distribution function (CDF) of the following parameters [15]:

- *SNF DEF EMPL*: The EMPL between the true defective radome SNF and that of the CS reconstructed defective radome SNF.
- *FF DEF EMPL*: The EMPL between the true defective radome FF and that of the CS reconstructed defective radome FF.
- *FF gold to recovered DEF EMPL*: The EMPL between the gold radome FF and that of the CS reconstructed defective radome FF.
- *FF gold to true DEF EMPL*: The EMPL between the gold radome FF and that of the true defective radome FF, which is a constant value across all the 50 sample sets used.

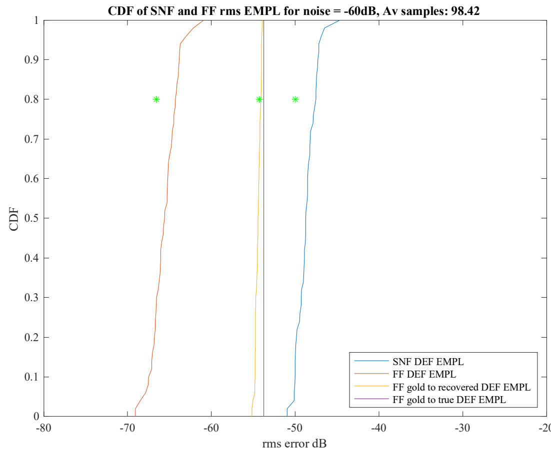


Fig. 8. CDF over 50 runs for the case of two radome patch faults of -1dB and 45°. Average number of CS samples of the SNF per run is 98.4. Simulation of SNF measurement untaken with -60dB of noise. Each of the four parameters are described in the text.

The results of Figure 8 show that the *SNF DEF EMPL* (blue) has an 80% CDF value of -47.5 dB which is a little worse that the case for a single radome patch fault as the CS algorithm has to work harder as the resulting difference field on the radome is less sparce. The 80% CDF result for *FF DEF EMPL* (red) is -64.3 dB and is a manifestation of the SNF transform gain effect. The 80% CDF value of the *FF gold to recovered DEF EMPL* (yellow) lays encouraging close to the true value of *FF gold to true DEF EMPL* (magenta) in the figure.

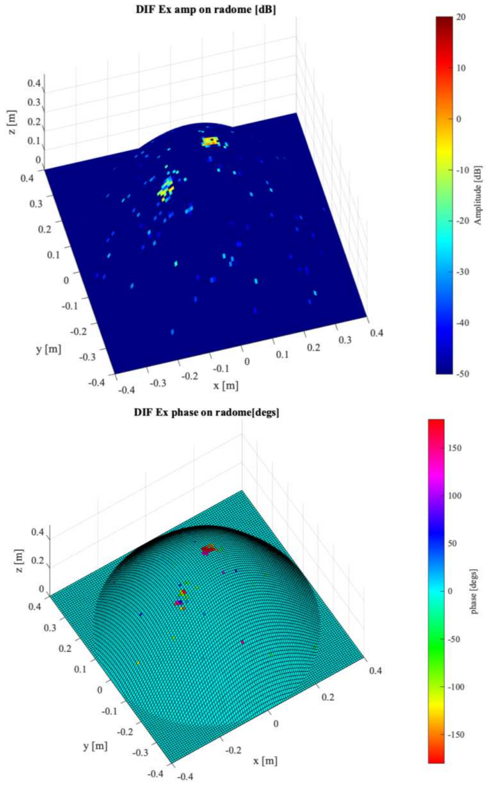


Fig. 9. A single result taken from figure 8 showing the CS reconstructed amplitude and phase of the $E_x$ difference field on the radome, two fault case.

As in illustration of the results of one set of these 50 runs, Figure 9 shows the CS reconstructed amplitude and phase of the $E_x$ difference field on the radome showing the correct location of the two patch faults. Figure 10 shows a comparison of the equivalent transformed FF radiation patterns of the gold and true defective radomes (top) and the corresponding result of the case of gold and reconstructed defective radomes (bottom).

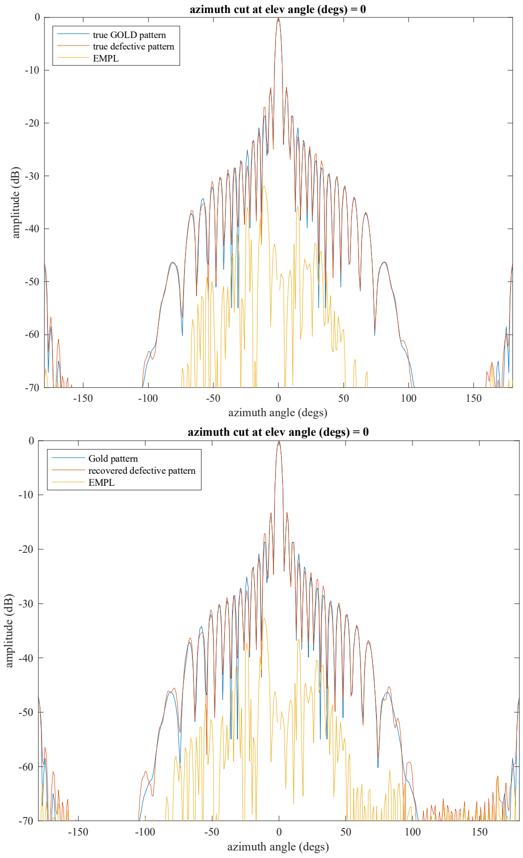


Fig. 10. A single result taken from figure 8 showing the azimuth FF radiation patterns of the gold and true defective radomes (top), and the gold and reconstructed defective radomes (bottom). EMPL values are shown in yellow.

## V. Summary and Conclusions

Building on our previous work of formulating the EC total-difference based CS process for the case of SNF measurements of ‘gold’ and faulty arrays [17], we have applied the technique to the case of detecting the location of faults on a radome surface using SNF difference field measurements of the gold and ‘faulty’ radome. Although the method does not allow calibration of the exact amplitude and phase fault on the radome, the location of the fault *is* correctly identified and most importantly the defective SNF and corresponding FF radiation pattern are accurately reconstructed using just 100 samples to an FF EMPL accuracy of better than -60 dB. We are currently undertaking an experimental verification of this technique using a commercial airliner radome excited by a weather radar using the robotic system shown in Figure 1 and plan to report the results of this work at the conference.

## References


[1] D.M. Lewis, J. Bommer, G.E. Hindman, S.F. Gregson, "Traditional to modern antenna test environments: The impact of robotics and computational electromagnetic simulation on modern antenna measurements," 15th European Conference on Antennas and Propagation (EuCAP), 2021

[2] D. Novotny, *et al*, “Performance evaluation of a robotically controlled millimeter-wave near-field pattern range at the NIST”, 2013 7th European Conference on Antennas and Propagation

[3] J. Guerrieri, et al, “Configurable Robotic Millimeter-Wave Antenna Facility”, 2015, 9th European Conference on Antennas and Propagation.

[4] J Guerrieri, et al, “Validation of Robotics for Antenna Measurements”, 2017 11th European Conference on Antennas and Propagation.

[5] D. R. Novotny, J. A. Gordon, M. S. Allman, “The Multi-Robot Large Antenna Positioning System for Over- The-Air Testing at the National Institute of Standards and Technology”, Proceedings of the AMTA Symposium.

[6] S.F. Gregson, D. Lewis, P. Schluper, G.E. Hindman, “Use of Model Based Systems Engineering and Development in the Design of a Commercial Nose-Radome Test System Employing a Multi-Axis Cobot”, 2024, 17th European Conference on Antennas and Propagation, Glasgow, UK.

[7] C.G. Parini, S.F. Gregson, J. McCormick, D. Janse van Rensburg, T. Eibert, “Theory and Practice of Modern Antenna Range Measurements 2nd Expanded Edition, Volume 1”, IET Electromagnetic Waves series 55 ISBN 978-1-83953-126-2, 2021.

[8] RTCA SC-173, "Change No. 1 to RTCA/DO-213 Minimum Operational Performance Standards For Nose-Mounted Radomes" RTCA, Inc., www.rtca.org, 1995.

[9] RTCA SC-230, "RTCA/DO-220A, Minimum Operational Performance Standards (MOPS) for Airborne Weather Radar Systems”, RTCA, Inc., www.rtca.org, 2016.

[10] RTCA SC-230, "RTCA/DO-213A Minimum Operational Performance Standards For Nose-Mounted Radomes," RTCA, Inc., www.rtca.org, 2016.

[11] L. C. Potter, E. Ertin, J. T. Parker, and M. Cetin, “Sparsity and compressed sensing in radar imaging,” Proc. IEEE, vol. 98, no. 6, pp. 1006–1020, 2010.

[12] M. Salucci, M. D. Migliore, P. Rocca, A. Polo and A. Massa, “Reliable antenna measurements in a near-field cylindrical setup with a sparsity promoting approach,” *IEEE Trans. Antennas Propag.*, vol. 68, no. 5, pp. 4143-4148, May 2020

[13] R. Cornelius, D. Heberling, N. Koep, A. Behboodi and R. Mathar, “Compressed sensing applied to spherical near-field to far-field transformation,” in *Proc. European Conf. Antennas Propag. (EuCAP),* Davos, Switzerland, 2016, pp. 1-4.

[14] Z. Chen, S.F. Gregson, Y. Wang, “Novel Application of Compressed Sensing in Cylindrical Mode Filtering for Far-Field Antenna Measurements”, Antenna Measurement Techniques Association Annual Symposium, October 2023, Seattle, USA.

[15] S.F. Gregson, Z. Qin, C.G. Parini, “Compressive Sensing in Massive MIMO Array Testing: A Practical Guide”, IEEE Transactions on Antennas and Propagation, 2022, Volume: 70, Issue: 9.

[16] C.G. Parini, S.F. Gregson, “Compressive Sensing Applied to Planar Near-Field Based Array Antenna Diagnostics for Production Testing”, AMTA 2023, October 2023, Seattle, USA.

[17] C.G. Parini, S.F. Gregson “Recent Advances in Compressive Sensing for Production Test and Antenna Diagnostics of 5G Massive MIMO Antennas”, 46th Annual AMTA Symposium, October 2024, Cincinnati, Kentucky, USA.